Intrinsic insulating ferromagnetism in manganese oxide thin films

Y. S. Hou, H. J. Xiang,[*] and X. G. Gong[†]

*Key Laboratory of Computational Physical Sciences (Ministry of Education), State Key Laboratory of Surface Physics,
and Department of Physics, Fudan University, Shanghai 200433, People's Republic of China*

By combining genetic algorithm optimizations, first-principles calculations and the double-exchange model studies, we have revealed that the exotic insulating ferromagnetism in LaMnO$_3$ thin film originates from the previously unreported G-type $d_{3z^2-r^2}/d_{x^2-y^2}$ orbital ordering. An insulating gap opens as a result of both the orbital ordering and the strong electron-phonon coupling. Therefore, there exist two strain-induced phase transitions in the LaMnO$_3$ thin film, from the insulating A-type antiferromagnetic phase to the insulating ferromagnetic phase and then to the metallic ferromagnetic phase. These phase transitions may be exploited in tunneling magnetoresistance- and tunneling electroresistance-related devices.

I. INTRODUCTION

Perovskite LaMnO$_3$ (LMO), a fundamental, strongly correlated electron system and the parent compound of the colossal magnetoresistance manganites, displays a complex correlation among structural, orbital, magnetic, and electronic degrees of freedom and has been extensively studied over the past decades [1]. Recently, LMO thin films have attracted considerable attention not only because many interesting and emerging phenomena have been discovered in LMO thin film-related superlattices [2–5] but also because LMO thin films display exotic behavior that is different from that of bulk. Experiments discovered a surprising insulating ferromagnetic (FM) phase in LMO thin films epitaxially grown on the square-lattice SrTiO$_3$ (STO) substrate [2,6–12]. The origin of this puzzling insulating FM phase is unclear. The unexpected ferromagnetism was considered to be extrinsic, and deficiency of La [9,13] was suggested as a possible explanation for it. However, it is not consistent with the tendency of the FM phase in LMO thin films with cation deficiency to be metallic [6,14,15]. Previous models [16,17] and recent first-principles studies [18,19] on LMO thin films predicted the metallic FM phase instead of the experimentally observed insulating FM phase. It is important to address how the prototypical antiferromagnetic (AFM) Mott insulator transforms to an insulating ferromagnet.

To address such an intriguing issue, we present a comprehensive theoretical paper on the LMO thin film by combining genetic algorithm (GA) optimizations, first-principles calculations, and orbital-degenerate double-exchange (DE) model studies. Our extensive GA simulations give an insulating FM phase of the LMO thin film, which crystallizes in the monoclinic $P21/n$ structure. This monoclinic $P21/n$ structure has a peculiar arrangement pattern of Jahn-Teller (JT) distortions of MnO$_6$ octahedra, giving rise to the previously unreported three-dimensionally $d_{3z^2-r^2}/d_{x^2-y^2}$−alternated orbital order. According to the Goodenough-Kanamori rules [20], this kind of orbital orders induces three-dimensional ferromagnetism. First-principles calculations show that the band gap of the

monoclinic $P21/n$ FM phase is 0.16 eV, compatible with the experimentally observed excitation energy [2] ($\approx$0.14 eV). Through the orbital-degenerate DE model, it is revealed that the band gap opens as a result of both the orbital ordering and the strong electron-phonon coupling. We also show that LMO thin film transforms from the insulating A-type antiferromagnetic (A-AFM) phase to the insulating FM phase and then to the metallic FM phase when the lateral lattice constant decreases.

II. COMPUTATIONAL DETAILS

In this paper, the widely adopted global optimization technique GA [21–24] is used to search the ground state structure of the LaMnO$_3$ thin film. The GA method we employed here is similar to that described in Ref. [24] with the exception that the spin information of the magnetic ions is explicitly kept in the crossover operation and a mutation operation related to the spin direction is added. A $\sqrt{2} \times \sqrt{2} \times 2$ perovskite supercell containing 4 formula units (f.u.; 20 atoms) is used. In GA searches, in order to match the experimentally epitaxial strain induced by the square-lattice substrate SrTiO$_3$, the two in-plane lattice vectors are fixed at $a_{\text{LMO}} = b_{\text{LMO}} = \sqrt{2}a_{\text{STO}}$ where a_{STO} is the lattice constant (3.905 Å) of the cubic STO substrate. However, both the length and the direction of the out-of-plane lattice vector c_{LMO} and the internal ionic coordinates are fully optimized.

First-principles calculations based on density functional theory (DFT) are performed using the generalized gradient approximation (GGA) with the PW91 parameterization as implemented in Vienna *Ab initio* Simulation Package (VASP) [25–28]. The projector-augmented wave method, an energy cutoff of 500 eV, and a k-point mesh grid of $7 \times 7 \times 5$ centered at the gamma point are used. The ions are relaxed towards equilibrium positions until the Hellmann-Feynman forces on each atoms are less than 0.01 eV/Å in structure relaxations. We use the rotationally invariant coulomb-corrected local spin density approximation (LSDA+U) method according to Liechtenstein *et al.* [29] with the experimentally deduced on-site coulomb energy [30] $U = 3.5$ eV applied to the manganese d electrons. The effect of U on our results will also be discussed later.

---

[*]hjxiang@fudan.edu.cn
[†]xggong@fudan.edu.cn

III. RESULTS AND DISCUSSIONS

We first reproduce the properties of bulk LaMnO$_3$ to ensure the validity of our calculation methods and U parameters. Then we use the GA optimization method to search the magnetic ground state of LMO thin films strained on SrTiO$_3$ and find that the ground state of LMO-strained thin films intrinsically adopts the experimentally observed insulating FM phase. We investigate the properties of this newly found insulating FM phase, including its crystal structures, band structures, and orbital orderings, to understand magnetic interactions in this system. Finally, orbital degenerate DE model studies are conducted to unveil the physical mechanism of the insulating ferromagnetism.

A. Reproduction of the magnetic ground state of bulk LMO

With the experimentally deduced [30] $U = 3.5$ eV and $J = 0.9$ eV applied to the Mn $3d$ electrons, our full
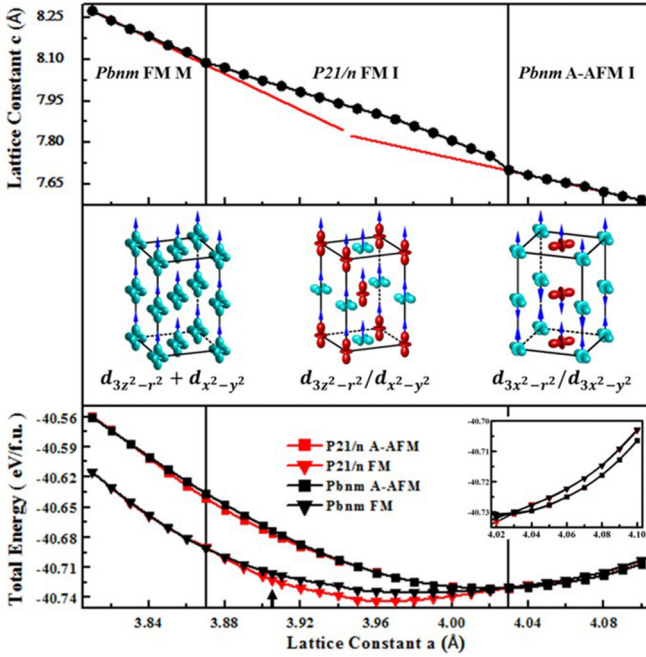

FIG. 1. (Color online) Calculated phase diagram of LaMnO$_3$ thin films. Within the considered lattice constant window, LMO thin films transform from *Pbnm* FM M to *P*21/*n* FM I and then to the *Pbnm* A-AFM I phases. LMO thin films with an NN Mn-Mn distance close (or equal) to that of bulk LMO [40] ($a = 3.99$ Å) do not take the bulk structure, because in this case LMO thin film is slightly stretched along the *a* axis and seriously compressed along the *b* axis. The evolution of the lattice constant *c* of the ground state is given in the upper panel. The two red straight lines are guides to the eyes. The magnetic and orbital orders of each ground state are depicted in the middle panel. Blue arrows represent spins. The bottom panel gives the total energies of the *P*21/*n* A-AFM, *P*21/*n* FM, *Pbnm* A-AFM, and *Pbnm* FM phases as a function of the square-lattice substrate lattice constant *a*. The black arrow indicates the lattice constant of the STO substrate. The *P*21/*n* FM phase merges with the *Pbnm* FM phase when the lattice constant becomes smaller than 3.88 Å, and the *P*21/*n* structure merges with the *Pbnm* structure when the lattice constant becomes larger than 4.03 Å.
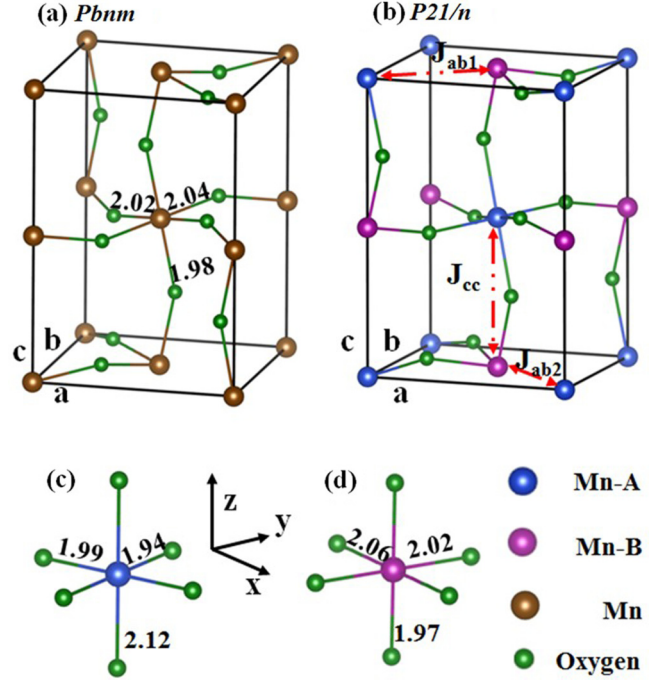

FIG. 2. (Color online) Structure of LaMnO$_3$ thin films strained on SrTiO$_3$. (a) Structure of the *Pbnm* FM M phase. (b) Structure and magnetic interaction paths J_{cc}, J_{ab1}, and J_{ab2} of the *P*21/*n* FM I phases. MnO$_6$ octahedra of Mn-A and Mn-B of the *P*21/*n* FM I phase are shown in (c) and (d), respectively. The local coordinate systems shown between (c) and (d) are chosen in such a way that the local *z* axis is nearly along the *c* axis and the *xy* plane is nearly in the *ab* plane. Crystallographic axes are given by *a*, *b*, and *c*. Allnumbers give Mn-O bond lengths in angstrom units.

structural optimizations successfully reproduce the A-AFM magnetic ground state in the bulk LMO with a lower total energy than the FM state by 8.5 meV/f.u., although it is not a trivial task to achieve this within DFT framework [31]. The calculated direct gap is 1.2 eV, consistent with optical measurements [32]. Besides, the relevant magnetic exchange constants are calculated to be $J_{ab} = 2.09$ meV and $J_c = -1.13$ meV. They are consistent with experimentally measured [33] $J_{ab} = 1.85$ meV and $J_c = -1.1$ meV. With these calculated magnetic exchange constants, Monte Carlo (MC) simulations reveal that the transition temperature is $T_N = 116$ K, consistent with the experimentally observed one [34] of $T_N = 140$ K. Intriguingly, our systematical studies show that either too small or too large U cannot correctly obtain the A-AFM magnetic ground state. We find that U should be between 2.5 and 4.0 eV to reproduce the A-AFM ground state. Unless specified, a U value of 3.5 eV is used for the following results.

B. Intrinsic insulating ferromagnetism in LMO thin films

Previously, LMO thin film strained on STO was always calculated to be metallic FM, with *Pbnm* symmetry, in contrast to the experimentally observed results. How insulating ferromagnetism arises in this system has always been a mystery to both theorists and experimentalists. Through extensive GA

searches, however, we find that an insulating FM phase, which has a total energy lower than the metallic *Pbnm* FM (*Pbnm* FM M) phase by 6.9 meV/f.u. (Fig. 1), is actually the magnetic ground state of this strained LMO thin film, making insulating ferromagnetism an intrinsic property of this system. To understand its magnetic interactions, the crystal structure, band structure, and orbital orderings of this newly found phase are investigated in this part.

This insulating FM phase crystallizes in a slightly distorted monoclinic $P21/n$ structure with $\beta = 90.74°$. Two kinds of Mn ions, denoted as Mn-A and Mn-B, are found in the monoclinic $P21/n$ structure [Fig. 2(b)], while all Mn ions are equivalent in the orthorhombic *Pbnm* structure [Fig. 2(a)]. Mn-A has a MnO_6 octahedron elongated along the c axis [Fig. 2(c)], while Mn-B has a MnO_6 octahedron stretched in the ab plane [Fig. 2(d)]. What is most significant is that these two kinds of Mn atoms are arranged in a checkerboard G-type manner [Fig. 2(b)]. This is rather different from the bulk LMO, where the relevant Q_3 modes [1] of the JT distortions of all MnO_6 octahedra are with their principal axes lying within the ab plane and these axes are alternatively arranged in this plane.

The band structure of the majority spin (up) of the monoclinic $P21/n$ FM phase is plotted in Fig. 3(a). The monoclinic $P21/n$ FM phase is insulating ($P21/n$ FM I). It has an indirect band gap of 0.16 eV, compatible with the experimentally observed excitation energy [2] (≈ 0.14 eV). Moreover, its bandwidth is narrower than that of the *Pbnm* FM M phase [Fig. 3(c)]. We expect that the $P21/n$ FM I

phase can be confirmed by the angle-resolved photoemission spectroscopy experiment.

We now examine the orbital order in the $P21/n$ FM I phase. Since the MnO_6 octahedron of Mn-A is elongated along the c axis, the $d_{3z^2-r^2}$ orbital is lower in energy than the $d_{x^2-y^2}$ orbital; thus, the single e_g electron occupies the $d_{3z^2-r^2}$ orbital, which can be shown by the partial density of states (PDOS) [Fig. 4(a)]. The notable split between the peak of the $d_{3z^2-r^2}$ orbital and that of the $d_{x^2-y^2}$ orbital is consistent with the large JT distortion [1] $Q_A = \sqrt{Q_2^2 + Q_3^2} = 0.27$ Å. In contrast, the orbital occupation is opposite for Mn-B. The $d_{x^2-y^2}$ orbital is lower in energy as a result of the in-plane stretch of the MnO_6 octahedron; thus, the single e_g electron mainly occupies the $d_{x^2-y^2}$ orbital, which can be verified by the PDOS [Fig. 4(b)]. Likewise, its relative weak split between the peak of the $d_{3z^2-r^2}$ orbital and that of the $d_{x^2-y^2}$ orbital is due to the small JT distortion $Q_B = \sqrt{Q_2^2 + Q_3^2} = 0.14$ Å. Figure 3(b) shows the e_g charge density integrated from -1.5 eV to the Fermi level, which displays the orbital order of the $P21/n$ FM I phase. In this energy interval, the spectral density of Mn-A has a predominantly $d_{3z^2-r^2}$ character, while Mn-B has a predominantly $d_{x^2-y^2}$ character. Therefore, we first report that the $P21/n$ FM I phase has a type of three-dimensionally $d_{3z^2-r^2}/d_{x^2-y^2}$−alternated orbital order, which is different from the $d_{3z^2-r^2} + d_{x^2-y^2}$ type [17] [Fig. 3(d)] and completely different from the $d_{3x^2-r^2}/d_{3y^2-r^2}$ type [35].

Based on the established orbital order, the magnetic interactions among the Mn atoms in the $P21/n$ FM I phase can be
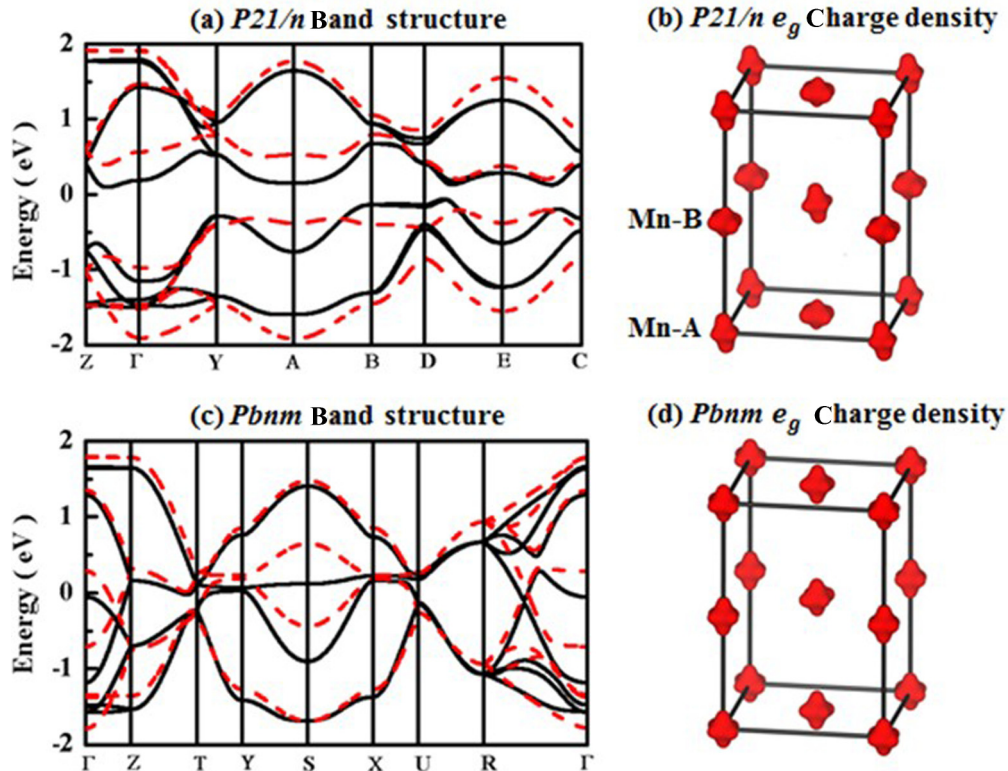

FIG. 3. (Color online) Band structure and charge density of $LaMnO_3$ film strained on $SrTiO_3$. Band structures of the $P21/n$ FM I and the *Pbnm* FM M phases are shown in (a) and (c), respectively. Black solid and red dashed lines in both (a) and (c) are from the DFT calculations and orbital-degenerate DE model, respectively. The Fermi level is set to zero. DFT calculated e_g charge density distributions of the $P21/n$ FM I and the *Pbnm* FM M phases in the energy window of 1.5 eV widths just below the Fermi level are plotted in (b) and (d), respectively.
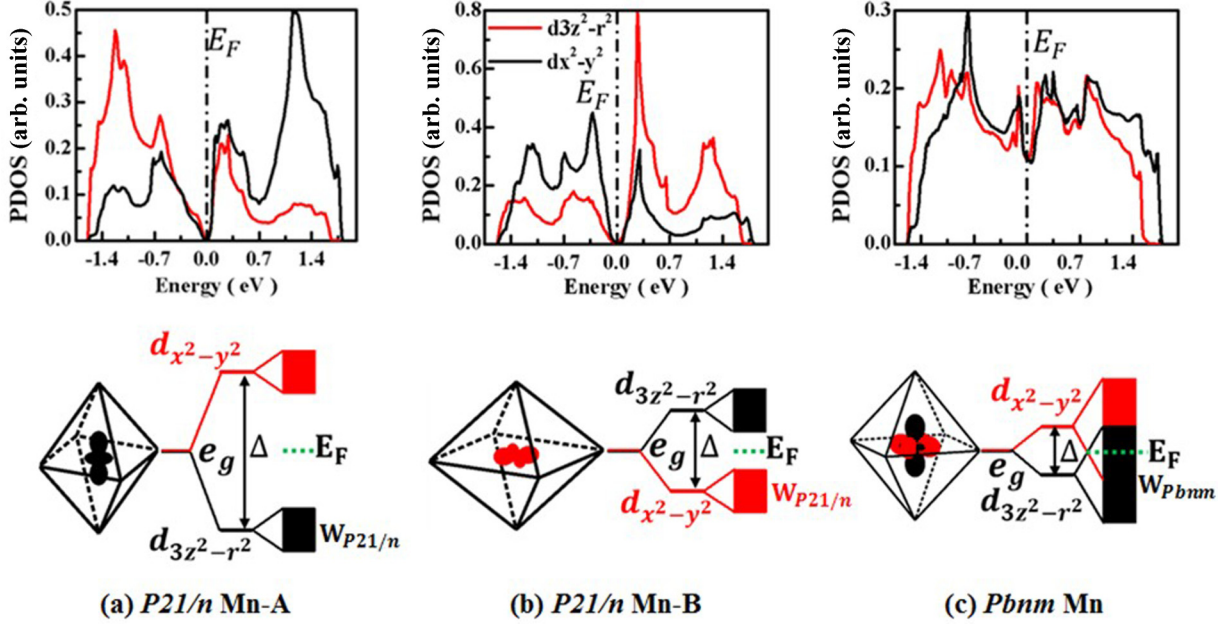
FIG. 4. (Color online) The PDOS and on-site energy splitting of LaMnO$_3$ thin film strained on SrTiO$_3$. The PDOS of Mn-A and Mn-B of the $P21/n$ FM I phase and the Mn atom of the $Pbnm$ FM M phase are shown in the upper panels of (a)–(c), respectively. The Fermi levels are indicated by the black vertical lines and are set to zero. Diagrammatic sketches of the on-site energy splitting of the two Mn-e_g orbitals shown in bottom panels of (a)–(c) correspond to Mn-A and Mn-B of the $P21/n$ FM I phase and the Mn atom of the $Pbnm$ FM M phase, respectively. The parameter Δ is the energy difference between the $d_{3z^2-r^2}$ and the $d_{x^2-y^2}$ orbitals. The black and red rectangular boxes represent the band derived from the $d_{3z^2-r^2}$ and $d_{x^2-y^2}$ orbitals, respectively, and the green horizontal lines indicate the Fermi levels.

deduced according to the Goodenough-Kanamori rules [20]. As a result of the three-dimensionally $d_{3z^2-r^2}/d_{x^2-y^2}$−alternated orbital order, the half-filled σ-bond $d_{3z^2-r^2}$ orbital from Mn-A overlaps with the empty σ-bond $d_{3z^2-r^2}$ orbital from Mn-B along the cubic [001] axis through the middle O-$2p_z$ orbital, giving rise to strong FM interactions. Besides, the half-filled π-bond t_{2g} orbitals will give rise to an AFM interaction between Mn-A and Mn-B. Since the overlap of the σ-bonding electrons is greater than that of the π-bonding electrons, the FM interaction turns out to be stronger than the AFM one. In other words, if Mn-A and Mn-B ferromagnetically interact along the [001] axis, the total energy is lowered significantly (upper panel of Fig. 5). If they interact antiferromagnetically, however, there is only a rather tiny energy gain (upper panel of Fig. 5) because not only the hybridization between the occupied $d_{3z^2-r^2}$ orbital of Mn-A and the unoccupied $d_{3z^2-r^2}$ orbital of Mn-B but also the π-type hybridizations between the t_{2g} orbital of Mn-A and the t_{2g} orbital of Mn-B are almost negligible. Therefore, the superexchange interaction between Mn-A and Mn-B along the cubic [001] axis is FM. This mechanism also applies to the magnetic interactions between Mn-A and Mn-B in the ab plane, where the mutually interacting orbitals are the half-filled σ-bonding $d_{x^2-y^2}$ orbital of Mn-B and the empty σ-bonding $d_{x^2-y^2}$ orbital of Mn-A. To sum up, Mn-A and Mn-B interact ferromagnetically along the [100], [010], and [001] axes (Fig. 5).

The deduced magnetic interactions among Mn atoms are verified by DFT calculations by means of the four-states mapping method [36]. The considered nearest-neighbor (NN) magnetic interaction paths J_{cc}, J_{ab1}, and J_{ab2} are shown in

Fig. 2(b). As expected, our calculations find $J_{cc} = 9.73$ meV, $J_{ab1} = 3.91$ meV, and $J_{ab2} = 5.94$ meV. All of them are FM. The next-nearest-neighbor magnetic interactions are found to be much weaker than the NN ones. Therefore, the magnetic ground state is FM. With the DFT-calculated magnetic exchange constants, our MC simulations lead to a transition temperature $T_C = 446$ K, higher than the experimentally measured ones [6,10] ranging from 115 K to 240 K. A possible explanation for this discrepancy is that the epitaxial strain is gradually relaxed from the substrate to the film surface; thus, the FM phase locates just near the strained film-substrate interface while the bulklike A-AFM phase dominates at the film surface, similar to the case of the strain-induced ferromagnetism in AFM LuMnO$_3$ thin film [37].

In addition, we find that our main results remain correct if a reasonable U value is used. Figure 6 shows that the monoclinic $P21/n$ state is always more stable than the $Pbnm$ state when a reasonable U between 2.5 and 4.0 eV that describes bulk LMO well is adopted. It is found that for U less than 2.0 eV, the monoclinic $P21/n$ state cannot be stabilized because the small U significantly underestimates the JT distortions. In other words, only the $Pbnm$ structure is obtained. For U larger than 3.0 eV, the $P21/n$ FM phase becomes insulating and has an appreciably lower total energy than the $Pbnm$ FM M phase. Moreover, both the band gap of the $P21/n$ FM I phase and the total energy difference between the $P21/n$ FM I and the $Pbnm$ FM M phases increase with U. Any U ranging from 1.0 to 6.0 eV cannot open a band gap in the $Pbnm$ FM phase.
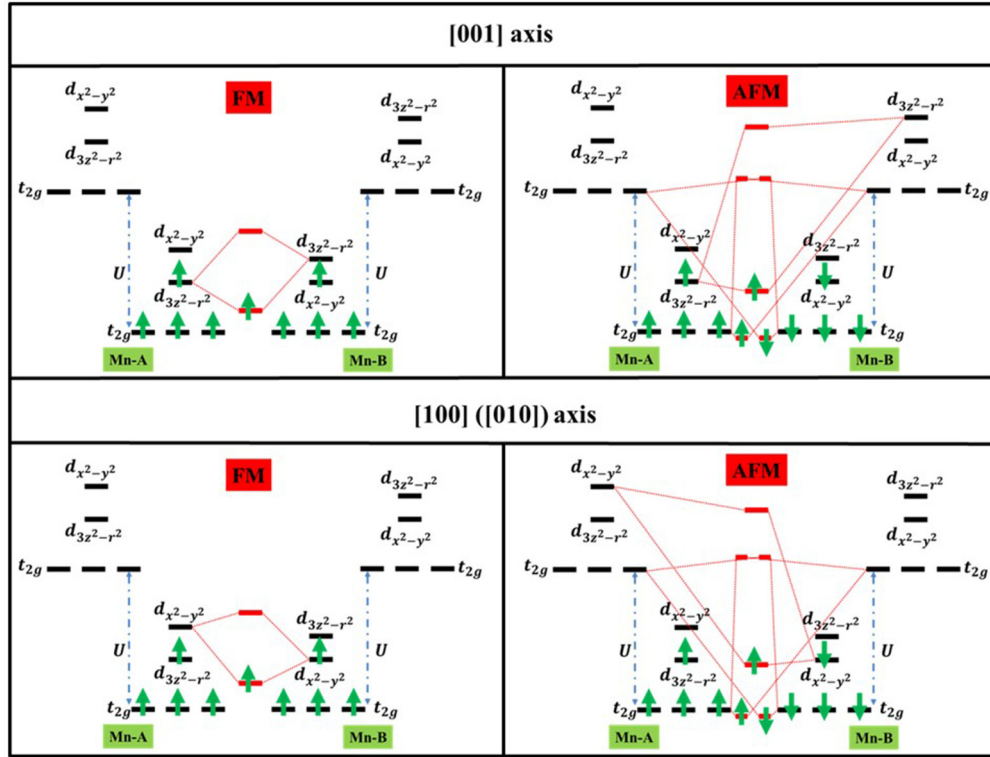
FIG. 5. (Color online) Orbital hybridizations between Mn-A and Mn-B with FM (left column) and AFM (right column) spin configurations, respectively. The upper panel is for the Mn pair along the [001] axis, while the bottom panel is for the in-plane Mn pair. Green arrows represent spins.
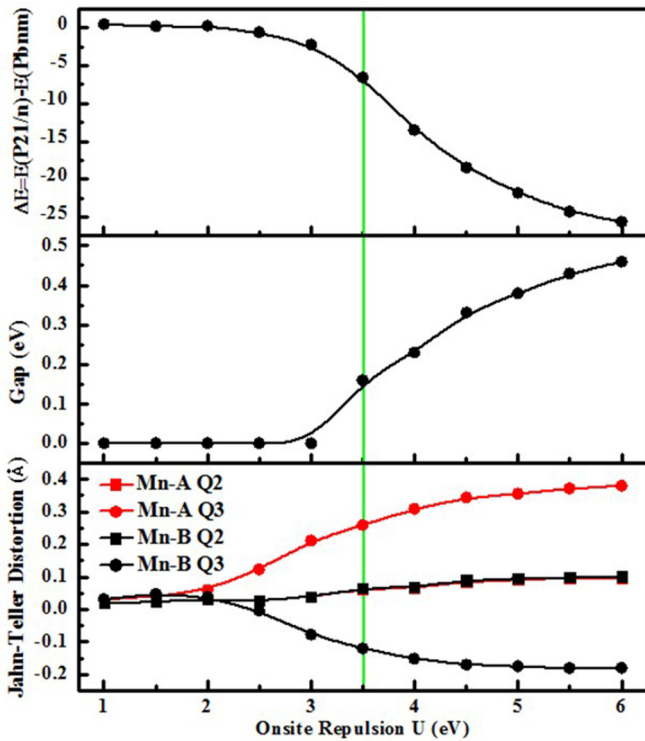

FIG. 6. (Color online) Dependence of the relative stability between the $P21/n$ FM and the $Pbnm$ FM M phases (upper panel), the band gap (middle panel), and the JT distortions (bottom panel) of the $P21/n$ FM phase on U.

C. Mechanism of the insulating ferromagnetism in the $P21/n$ phase

In order to unveil the mechanism of the insulating ferromagnetism, we employ the orbital-degenerate DE model with one e_g electron per Mn^{3+} ion. An infinite Hund coupling limit [1], i.e., $J_H = \infty$, is adopted in our paper. With this useful simplification, the DE model Hamiltonian reads

$$H = -\sum_{\langle ij \rangle}^{\alpha\beta} t_{\alpha\beta}^{\vec{a}} (\Omega_{ij} d_{i\alpha}^+ d_{j\beta} + H.C.) + \sum_{\langle ij \rangle} J_{AF}^{\vec{a}} \vec{S}_i \cdot \vec{S}_j$$

$$+ \lambda \sum_i (-Q_{1i} n_{1i} + Q_{2i} \tau_{xi} + Q_{3i} \tau_{zi})$$

$$+ \frac{1}{2} \sum_i \left(2Q_{1i}^2 + Q_{2i}^2 + Q_{3i}^2 \right). \tag{1}$$

In this Hamiltonian, $d_{i\alpha}^+$ and $d_{i\alpha}$ are the creation and annihilation operators, respectively, for the e_g electron on the orbital $\alpha = |x^2 - y^2\rangle (a)$ and $\beta = |3z^2 - r^2\rangle (b)$, with its spin parallel to the localized t_{2g} spin $\vec{S}_i$; $\vec{a} = \mathbf{x}, \mathbf{y}, \mathbf{z}$ is the direction of the link connecting the two NN Mn^{3+} sites; and Berry phase $\Omega_{ij} = \cos\frac{\theta_i}{2} \cos\frac{\theta_j}{2} + \sin\frac{\theta_i}{2} \sin\frac{\theta_j}{2} e^{-i(\phi_i - \phi_j)}$ arises due to the infinite Hund coupling, where θ and ϕ are the polar and azimuthal angles of the t_{2g} spins, respectively. In the model Hamiltonian, the first term is the standard DE interaction. The hopping parameters are $t_{aa}^x = -\sqrt{3} t_{ab}^x = -\sqrt{3} t_{ba}^x = 3t_{bb}^x = \frac{3t_0}{4}$, $t_{aa}^y = \sqrt{3} t_{ab}^y = \sqrt{3} t_{ba}^y = 3t_{bb}^y = \frac{3t_0}{4}$, $t_{aa}^z = t_{ab}^z = t_{ba}^z = 0$, and $t_{bb}^z = t_0$. The second term is the NN t_{2g} spin interaction

through the AFM superexchange $J_{AF} > 0$. The third term is the electron-phonon coupling, where λ is a dimensionless constant and the e_g-orbital operators are $n_i = d_{ia}^+ d_{ia} + d_{ib}^+ d_{ib}$, $\tau_{xi} = d_{ia}^+ d_{ib} + d_{ib}^+ d_{ia}$, and $\tau_{zi} = d_{ia}^+ d_{ia} - d_{ib}^+ d_{ib}$. The last term is the lattice elastic energy. The JT modes (Q_2 and Q_3) and breathing mode (Q_1) are defined in Ref. [1].

In the present paper, the NN AFM superexchange interaction between Mn t_{2g} spins, i.e., the second term, is left out of considerations since both the $P21/n$ and the $Pbnm$ phases are FM. The DFT relaxed structures of the $P21/n$ FM and the $Pbnm$ FM phases are used. Because the breathing modes (Q_1) are much smaller than the JT modes (Q_2 and Q_3) in both phases, they are ignored in our paper. Lastly, $t_0 = 0.52$ eV and $\lambda = 1.4$ (λ usually estimated [1] between 1.0 and 1.6) are used [38,39]. This set of parameters results in an energy difference between the $P21/n$ FM and the $Pbnm$ FM phases close to that obtained from the DFT calculations. By exactly diagonalizing the DE Hamiltonian, we show the band structures of the $P21/n$ FM and the $Pbnm$ FM phases in Figs. 3(a) and 3(c), respectively. As expected, the band structure of the $P21/n$ FM phase is characteristic of an insulator and that of the $Pbnm$ FM phase is characteristic of a metal. The profiles of both band structures obtained from the model well reproduce that obtained from the DFT calculations, indicating that the parameters involved in the model are appropriately selected.

Let's address why the $P21/n$ FM phase is insulating while the $Pbnm$ FM phase is metallic. For the $P21/n$ FM phase, because the three-dimensionally $d_{3z^2-r^2}/d_{x^2-y^2}$-alternated orbital order has almost no overlap along the c axis ($t_{ab}^z = t_{ba}^z = 0$) between the occupied orbitals, its bandwidth $W_{P21/n}$ is determined mainly by the in-plane overlap ($t_{ab}^x = t_{ba}^x = -\frac{\sqrt{3}}{4}t_0$ or $t_{ab}^y = t_{ba}^y = \frac{\sqrt{3}}{4}t_0$) between the lower-energy occupied orbital $d_{3z^2-r^2}$ of Mn-A and the lower-energy occupied orbital $d_{x^2-y^2}$ of Mn-B. So its bandwidth $W_{P21/n}$ is proportional to $\sqrt{3}t_0$. Likewise, the bandwidth W_{Pbnm} of the $Pbnm$ FM phase determined by the $d_{3z^2-r^2} + d_{x^2-y^2}$-type orbital order is proportional to $3t_0$. Thus, the $P21/n$ FM phase has a narrower bandwidth than the $Pbnm$ FM phase. However, the on-site energy splitting of the two Mn-e_g orbitals due to the electron-phonon coupling in an isolated MnO$_6$ octahedron is proportional to the strength of the JT distortions [18]:

$$\epsilon_\pm = \pm\lambda\sqrt{Q_2^2 + Q_3^2}. \tag{2}$$

Thus, the on-site energy splitting in the $P21/n$ FM phase is much larger than that in the $Pbnm$ FM phase, because the JT distortions in the former are much severer than those in the latter. Therefore, the $P21/n$ FM phase possesses a finite band gap as a result of the narrow bandwidth and the large on-site e_g-level splitting [Figs. 4(a) and 4(b)]. For the $Pbnm$ FM phase, however, its bandwidths of Mn-e_g bands are so wide and the electron-phonon coupling is so weak that no band gap opens [Fig. 4(c)]. Furthermore, decompositions of the total energies of both phases (Table I) show that the electron-phonon coupling causes a much larger energy lowering in the $P21/n$ FM phase than in the $Pbnm$ FM phase, although the $P21/n$ FM phase has higher hopping energy and lattice elastic energy than does the $Pbnm$ FM phase. In conclusion, it is revealed that the orbital order and the electron-phonon coupling cooperatively

TABLE I. Decompositions of the total energies (E_{tot}) of the $P21/n$ FM I and the $Pbnm$ FM M phases (20 atoms, i.e., 4 f.u.) into the hopping energy ($E_{hopping}$), electron-phonon coupling (E_{ele-ph}), and lattice elastic energy ($E_{lattice}$).

	$E_{hopping}$ (eV)	E_{ele-ph} (eV)	$E_{lattice}$ (eV)	E_{tot} (eV)
$P21/n$	−2.4354	−1.5878	0.9045	−3.1187
$Pbnm$	−3.0319	−0.1978	0.1332	−3.0966

make the $P21/n$ FM phase insulating, whereas they make the $Pbnm$ FM phase metallic, and that the electron-phonon coupling plays a vital role in stabilizing the $P21/n$ FM I phase as the ground state of the LMO thin film strained on STO.

D. Property dependence of LMO thin films on lattice constants

Using the same strategy applied to the LMO thin film strained on STO, we have systematically investigated the property dependence of LMO thin films on lattice constants, which can be experimentally tuned by selecting different square-lattice substrates. Here, only the $P21/n$ and $Pbnm$ space groups are considered. As usual, several common magnetic orders in perovskite are considered, i.e., FM, A-AFM, C-type AFM (C-AFM), and G-type AFM (G-AFM) spin orderings. The FM and A-AFM results are shown in Fig. 1. As the C-AFM and G-AFM spin orders do not appear as the lowest energy phase in the considered lattice constant window, they are not shown in Fig. 1 and not further discussed. Our results show that LMO thin films with lattice constants ranging from 3.88 to 4.03 Å are insulating ferromagnetism with the monoclinic $P21/n$ structure and the three-dimensionally $d_{3z^2-r^2}/d_{x^2-y^2}$-alternated orbital order. However, LMO thin films with lattice constants smaller than 3.88 Å are metallic ferromagnetism with the $Pbnm$ structure and $d_{3z^2-r^2} + d_{x^2-y^2}$-type orbital order. When the lattice constant is larger than 4.04 Å, the ground state of the LMO thin films becomes the $Pbnm$ structure with an insulating A-AFM order and $d_{3x^2-r^2}/d_{3y^2-r^2}$-type orbital order. The $Pbnm$ FM M and the insulating $Pbnm$ A-AFM ($Pbnm$ A-AFM I) phases are consistent with the paper by Lee *et al.* [19] on LMO thin film with large compressive and tensile epitaxial strain. The phase transitions from the $P21/n$ FM I phase to the $Pbnm$ FM M phase and then to the $Pbnm$ A-AFM I phase are intuitively illustrated by the obvious discontinuity of the lattice constant c, shown in the upper panel of Fig. 1. The phase diagram shown in Fig. 1 is also confirmed by our GA optimizations.

IV. SUMMARY

The physical origin of the well-known and puzzling insulating ferromagnetism experimentally observed in the LaMnO$_3$ thin film grown on the square-lattice SrTiO$_3$ substrate has been investigated. We find that the insulating FM phase is intrinsically from strain-induced orbital ordering, instead of extrinsic reasons such as defects. It crystallizes in a monoclinic $P21/n$ structure, which has two kinds of MnO$_6$ octahedra: One is elongated along the c axis, and the other one is stretched in the ab plane. They are arranged in a checkerboard G-type manner, giving rising to a previously unreported

three-dimensionally $d_{3z^2-r^2}/d_{x^2-y^2}-$alternated orbital order, which naturally leads to the ferromagnetism. The DE model reveals that the band gap opens due to both the orbital ordering and the strong electron-phonon coupling. Finally, we find that epitaxially strained LMO thin film transforms from the insulating A-AFM phase to the insulating FM phase and then to the metallic FM phase when the lateral lattice constant decreases. If LMO thin film is epitaxially grown on some specified piezoelectric materials, an electric-field-induced metal-insulator transition and an electric field control of the magnetism can be realized experimentally at $Pbnm$ FM M $\rightarrow P21/n$ FM I and $P21/n$ FM I $\rightarrow Pbnm$ A-AFM I phase boundaries, respectively. These electric-field-induced phase transitions may be exploited in tunneling magnetoresistance- and tunneling electroresistance-related devices.

[1] E. Dagotto, T. Hotta, and A. Moreo, Phys. Rep. **344**, 1 (2001).

[2] A. Bhattacharya, S. J. May, S. G. E. te Velthuis, M. Warusawithana, X. Zhai, B. Jiang, J. M. Zuo, M. R. Fitzsimmons, S. D. Bader, and J. N. Eckstein, Phys. Rev. Lett. **100**, 257203 (2008).

[3] J. Garcia-Barriocanal, J. C. Cezar, F. Y. Bruno, P. Thakur, N. B. Brookes, C. Utfeld, A. Rivera-Calzada, S. R. Giblin, J. W. Taylor, J. A. Duffy, S. B. Dugdale, T. Nakamura, K. Kodama, C. Leon, S. Okamoto, and J. Santamaria, Nat. Comm. **1**, 82 (2010).

[4] M. Gibert, P. Zubko, R. Scherwitzl, J. Iniguez, and J.-M. Triscone, Nat. Mater. **11**, 195 (2012).

[5] K. Rogdakis *et al.*, Nat. Comm. **3**, 1064 (2012).

[6] A. Gupta, T. R. McGuire, P. R. Duncombe, M. Rupp, J. Z. Sun, W. J. Gallagher, and G. Xiao, Appl. Phys. Lett. **67**, 3494 (1995).

[7] W. Choi *et al.*, J. Phys. D: Appl. Phys. **42**, 165401 (2009).

[8] C. Adamo, X. Ke, P. Schiffer, A. Soukiassian, M. Warusawithana, L. Maritato, and D. Schlom, Appl. Phys. Lett. **92**, 112508 (2008).

[9] Z. Marton, S. S. A. Seo, T. Egami, and H. N. Lee, J. Cryst. Growth **312**, 2923 (2010).

[10] H.-S. Kim and H. M. Christen, J. Phys.: Condens. Matter **22**, 146007 (2010).

[11] X. Zhai, C. S. Mohapatra, A. B. Shah, J.-M. Zuo, and J. N. Eckstein, J. Appl. Phys. **113**, 173913 (2013).

[12] W. S. Choi, D. W. Jeong, S. Y. Jang, Z. Marton, S. S. A. Seo, H. N. Lee, and Y. S. Lee, J. Korean Phys. Soc. **58**, 569 (2011).

[13] C. Aruta *et al.*, J. Appl. Phys. **100**, 023910 (2006).

[14] T. McGuire, A. Gupta, P. Duncombe, M. Rupp, J. Sun, R. Laibowitz, W. Gallagher, and G. Xiao, J. Appl. Phys. **79**, 4549 (1996).

[15] P. Orgiani, C. Aruta, R. Ciancio, A. Galdi, and L. Maritato, Appl. Phys. Lett. **95**, 013510 (2009).

[16] K. H. Ahn and A. J. Millis, Phys. Rev. B **64**, 115103 (2001).

[17] B. R. K. Nanda and S. Satpathy, Phys. Rev. B **81**, 174423 (2010).

[18] B. R. K. Nanda and S. Satpathy, J. Magn. Magn. Mater. **322**, 3653 (2010).

[19] J. H. Lee, K. T. Delaney, E. Bousquet, N. A. Spaldin, and K. M. Rabe, Phys. Rev. B **88**, 174426 (2013).

[20] J. B. Goodenough, *Magnetism and the Chemical Bond* (Interscience, New York, 1963).

[21] D. M. Deaven and K. M. Ho, Phys. Rev. Lett. **75**, 288 (1995).

[22] H. J. Xiang, S.-H. Wei, and X. G. Gong, Phys. Rev. B **82**, 035416 (2010).

[23] H. J. Xiang, S. H. Wei, and X. G. Gong, J. Am. Chem. Soc. **132**, 7355 (2010).

[24] X. Lu, X. Gong, and H. Xiang, arXiv:1308.0076.

[25] J. P. Perdew, J. A. Chevary, S. H. Vosko, K. A. Jackson, M. R. Pederson, D. J. Singh, and C. Fiolhais, Phys. Rev. B **46**, 6671 (1992).

[26] P. E. Blöchl, Phys. Rev. B **50**, 17953 (1994).

[27] G. Kresse and J. Furthmüller, Phys. Rev. B **54**, 11169 (1996).

[28] G. Kresse and D. Joubert, Phys. Rev. B **59**, 1758 (1999).

[29] A. I. Liechtenstein, V. I. Anisimov, and J. Zaanen, Phys. Rev. B **52**, R5467 (1995).

[30] J. H. Park, C. T. Chen, S. W. Cheong, W. Bao, G. Meigs, V. Chakarian, and Y. U. Idzerda, Phys. Rev. Lett. **76**, 4215 (1996).

[31] T. Hashimoto, S. Ishibashi, and K. Terakura, Phys. Rev. B **82**, 045124 (2010).

[32] T. Arima, Y. Tokura, and J. B. Torrance, Phys. Rev. B **48**, 17006 (1993).

[33] R. J. McQueeney, J. Q. Yan, S. Chang, and J. Ma, Phys. Rev. B **78**, 184417 (2008).

[34] E. O. Wollan and W. C. Koehler, Phys. Rev. **100**, 545 (1955).

[35] S. Dong, R. Yu, S. Yunoki, G. Alvarez, J. M. Liu, and E. Dagotto, Phys. Rev. B **78**, 201102 (2008).

[36] H. Xiang, C. Lee, H.-J. Koo, X. Gong, and M.-H. Whangbo, Dalton Trans. **42**, 823 (2013).

[37] J. S. White *et al.*, Phys. Rev. Lett. **111**, 037201 (2013).

[38] Z. Popovic and S. Satpathy, Phys. Rev. Lett. **84**, 1603 (2000).

[39] K. H. Ahn and A. J. Millis, Phys. Rev. B **61**, 13545 (2000).

[40] J. Rodriguez-Carvajal, M. Hennion, F. Moussa, A. H. Moudden, L. Pinsard, and A. Revcolevschi, Phys. Rev. B **57**, R3189 (1998).